The Astronomical Journal, 162:104 (16pp), 2021 September https://doi.org/10.3847/1538-3881/ac111d

Wavelength Dependence of Activity-induced Photometric Variations for Young Cool Stars in Hyades

Kohei Miyakawa[1], Teruyuki Hirano[2,3], Akihiko Fukui[4,5], Andrew W. Mann[6], Eric Gaidos[7], and Bun'ei Sato[1]
[1] Department of Earth and Planetary Sciences, Tokyo Institute of Technology, Meguro-ku, Tokyo, 152-8551, Japan; miyakawa.k.aa@m.titech.ac.jp
[2] Astrobiology Center, 2-21-1 Osawa, Mitaka, Tokyo 181-8588, Japan
[3] National Astronomical Observatory of Japan, NINS, 2-21-1 Osawa, Mitaka, Tokyo 181-8588, Japan
[4] Komaba Institute for Science, The University of Tokyo, 3-8-1 Komaba, Meguro, Tokyo 153-8902, Japan
[5] Instituto de Astrofísica de Canarias, Vía Láctea s/n, E-38205 La Laguna, Tenerife, Spain
[6] Department of Physics and Astronomy, The University of North Carolina at Chapel Hill, Chapel Hill, NC 27599, USA
[7] Department of Earth Sciences, University of Hawaii at Mānoa, Honolulu, HI 96822, USA
Received 2021 April 22; revised 2021 July 1; accepted 2021 July 1; published 2021 August 16

Abstract

We investigate photometric variations due to stellar activity that induce systematic radial-velocity errors (so-called "jitter") for the four targets in the Hyades open cluster observed by the K2 mission (EPIC 210721261, EPIC 210923016, EPIC 247122957, and EPIC 247783757). Applying Gaussian process regressions to the K2 light curves and the near-infrared (NIR) light curves observed with the IRSF 1.4 m telescope, we derive the wavelength dependences of the photometric signals due to stellar activity. To estimate the temporal variations in the photometric variability amplitudes between the two observation periods of K2 and IRSF, separated by more than 2 yr, we analyze a number of K2 targets in Hyades that have also been observed in Campaigns 4 and 13 and find a representative variation rate over 2 yr of $38\% \pm 71\%$. Taking this temporal variation into account, we constrain projected sizes and temperature contrast properties of the starspots in the stellar photosphere to be approximately 10% and 0.95%, respectively. These starspot properties can induce relatively large differences in the variability amplitude over different observational passbands, and we find that radial-velocity jitter may be more suppressed in the NIR than previously expected. Our result supports profits of ongoing exoplanet search projects that are attempting to detect or confirm young planets in open clusters via radial-velocity measurements in the NIR.

Unified Astronomy Thesaurus concepts: Multi-color photometry (1077); Exoplanet evolution (491); Starspots (1572); Late-type stars (909)

1. Introduction

Exoplanetary studies have made great progress with the help of space telescope missions such as NASA's Kepler space telescope (Borucki et al. 2010). In particular, Kepler's secondary mission, K2, conducted a systematic survey of young transiting planets in stellar clusters (<1 Gyr) that were not included in the original mission (e.g., Hyades (650 Myr, Martín et al. 2018), Pleades (112 Myr, Dahm 2015), and Upper Scorpius 11 Myr, Pecaut et al. 2012). Several planets have been confirmed and/or validated around these young stars (e.g., Mann et al. 2016a, 2016b, 2017), which are important to study to determine the formation and evolutionary processes of exoplanets, as well as their primordial atmospheres. More recently, an all-sky survey by the TESS mission (Ricker et al. 2015) also revealed young exoplanets in other stellar associations (e.g., Newton et al. 2019; Mann et al. 2020; Rizzuto et al. 2020).

Even though the sky regions being surveyed have expanded, the number of planets detected around young stars remains far more limited (∼30) than those around their older counterparts. One reason for the small number of detections are the high surface activities of these young host stars. When the brightness of the stellar surface is inhomogenious (e.g., includes spots and plages), apparent modulations due to stellar rotation appear in radial-velocity (RV) measurements. These activity-induced apparent signals, so-called "RV jitters," prevent the detection of true planetary signals (e.g., Queloz et al. 2001; Paulson et al. 2004). In particular, less is known concerning the properties of RV jitter for low-mass stars (M dwarfs) as a result of their intrinsic faintness, despite the fact that starspots tend to exist longer on M dwarfs than on solar-type stars and could affect their long-term RV variability (Robertson et al. 2014, 2020; Davenport et al. 2015). Recent studies have suggested that planetary radii around young stars are significantly larger than those around old stars in the low-mass region ($<0.6\,M_{\odot}$, e.g., Obermeier et al. 2016; Mann et al. 2018; Rizzuto et al. 2020). Studies of young low-mass stars are important to test for the scenarios that explain the difference in the radius distributions, including atmospheric escape (e.g., Owen 2019).

In general, it is known that RV jitter is reduced in the near-infrared (NIR) relative to optical wavelengths because the contrast between starspots and the photosphere is smaller at longer wavelengths (Bean et al. 2010; Reiners & Basri 2010; Anglada-Escudé et al. 2013; Tal-Or et al. 2018; Robertson et al. 2020). However, the number of observational samples available for systematic studies of stellar activity is still small and the detailed properties of starspots are concealed, especially for young M dwarfs. Measuring stellar RVs is one of the promising methods to study the detailed properties of jitter, such as their wavelength dependence (e.g., Robertson et al. 2020); however, it is time consuming to obtain a sufficiently large number of observations, especially for optically faint targets such as M dwarfs. Frasca et al. (2009) have approached this problem using photometric observations; however, their targets have been limited to pre-main-sequence stars (∼10 Myr) that show large photometric variations (>10%). Therefore, reduced jitter in the NIR and its wavelength dependence have not been robustly established for various types of stars of different

ages. For a more accurate understanding of young exoplanets, it is necessary to constrain the behavior of stellar rotational activity using both photometry and spectroscopy.

In this study, we evaluate the observational behavior of stellar rotational activity in the NIR. We focus on M dwarfs in the Hyades open cluster (650 Myr; Martín et al. 2018) that were photometrically observed by the K2 mission, and we investigate stellar jitter using multicolor photometry combining the K2 and NIR light curves. We also estimate the starspot sizes and temperatures using a toy model. Our approach allows us to roughly understand the properties of starspots for targets showing relatively small (∼1%) simple photometric variabilities with 1 m class telescopes.

This paper is organized as follows. In Section 2, we introduce our targets and follow-up observations using the NIR multicolor photometry. We show the analytic procedure for the targets involving Gaussian process regression in Section 3. Section 4 presents an estimation of the starspot properties. Finally, we discuss our interpretations of the results compared to previous studies and give a conclusion in Section 5.

2. Targets and Observations

2.1. K2 Targets in the Hyades Open Cluster

K2 is the secondary mission of the Kepler space telescope to detect transiting exoplanet candidates along the ecliptic plane (Howell et al. 2014). Some K2 campaign fields include young clusters. To reduce systematic effects when studying the properties of starspot, such as those associated with age and metallicity, we focused on young stars belonging to a single open cluster. We selected targets from the Hyades open cluster with typical metallicity [Fe/H] and age values of approximately 0.14 ± 0.05 Myr and 650 ± 70 Myr, respectively (Perryman et al. 1998; Brandt & Huang 2015; Martín et al. 2018).

We picked four preferable targets for ground-based follow-up observations that are relatively bright and have short rotation periods ($<10\,\mathrm{mag}_K$ and <3 days) from the VizieR table[8] reported in Douglas et al. (2019): EPIC 210721261, EPIC 210923016, EPIC 247122957, and EPIC 247783757. Transiting planetary candidates have not been detected for these targets. The K2 data were collected on Campaign 13, which was from 2017 March 8 to May 27. We use the Pre-search Data Conditioned-Simple Aperture Photometry light curves dowloaded from the Mikulski Archive for Space Telescopes portal.[9] For this study, we normalized the overall long-term systematic modulations using a fifth-order polynomial function and removed flux outliers via $5-\sigma$ clipping, to focus on periodic variations due to stellar rotation. We summarize the properties of the targets in Table 1. The stellar effective temperatures and radii are derived by $V-J$ versus $T_{\rm eff}$ relation and M_K versus R_* relation from Mann et al. (2015), respectively; the masses are by M_K versus $M_\star$ relation from Mann et al. (2019) with the metallicity of 0.15.

We also estimated the stellar properties using different equations because young active stars have large uncertainties in the colors due to their inhomogeneous surfaces (Stauffer et al. 2003). Additional estimations for $T_{\rm eff}$ and R_* using the $BP-RP$ versus $T_{\rm eff}$ and $T_{\rm eff}$ versus R_* relations, respectively (from Mann et al. 2015), are listed in the bottom of Table 1. These values deviate by about 1σ from the original estimations, which means that there are large uncertainties in the broadband colors. In addition, we checked the CaII HK (393.4 nm and 396.8 nm) and Hα (656.3 nm) emission lines as activity indicators using low-resolution spectra observed with the the Large Sky Area Multi-Object Fiber Spectroscopic Telescope (LAMOST; Cui et al. 2012).[10] The spectral data are available for EPIC 210721261, EPIC 210923016, and EPIC 247783757. All the three targets exhibit significant emissions at those lines as in Figure 1. Thus, we conclude that our targets are very active and it is possible that the systematic errors in the effective temperatures are underestimated. In later discussions, we will take into account this point to interpret the results more accurately.

2.1.1. Rotation Periods

For the selected target stars, we first investigated the periodic modulations in the K2 light curves and determined the rotation period for each target. To do so, we applied the generalized Lomb–Scargle periodogram (GLS; Zechmeister & Kürster 2009) to unbinned K2 light curves; the results are shown in Figure 2 with the black solid line. In addition, we computed the autocorrelation function (ACF; McQuillan et al. 2013) using the same data sets to confirm the periods identified in the GLS periodogram. For EPIC 210721261, EPIC 247122957, and EPIC 247783757, the same periods were detected by both GLS and ACF and we adopted these periods for the subsequent analyses. For EPIC 210923016, the highest peak was detected at 0.58 days in GLS. ACF, however, showed the highest peak at 1.16 days, which is twice the GLS period. The 0.58 days peak is an upper harmonic of 1.16 day and likely due to multiple starspots on the surface, and we concluded that 1.16 days is the true rotation period of the star. Finally, via visual inspection, we confirmed semicoherent modulations with the determined periods in the K2 light curves for all targets (Figure 5).

2.1.2. Possibility of Binary

Because we are trying to constrain the starspot properties (e.g., sizes and temperatures) from multicolor photometric observations, it is important to rule out the presence of nearby (companion) stars in the photometric aperture because; when a light curve is diluted by flux contamination from nearby stars, the interpretation of the amplitude of the light curve modulations is more complicated. To ensure of the absence of possible companion stars, we inspected nearby stars listed in the 2MASS (Cutri et al. 2003), SDSS (Adelman-McCarthy et al. 2009), and Gaia (Gaia Collaboration et al. 2018) catalogs on the VizieR website,[11] and found that there are no resolved companions within three. However, it is difficult to completely eliminate the possibility of binaries, because high-precision adaptive optic observations have not been performed. Therefore, to evaluate the binarity of the targets, we employed the thresholds described in Evans (2018) for the Astrometric Goodness of Fit in the Along–Scan direction (`GOF_AL`) and the Significance of the Astrometric Excess Noise (`D`) in the Gaia second data release (DR2; Gaia Collaboration et al. 2016, 2018). These parameters characterize the agreement

[8] https://vizier.u-strasbg.fr/viz-bin/VizieR-3?-source=J/ApJ/879/100/table3
[9] http://archive.stsci.edu/k2/epic/search.php
[10] http://dr6.lamost.org/v2/search
[11] http://vizier.u-strasbg.fr/viz-bin/VizieR

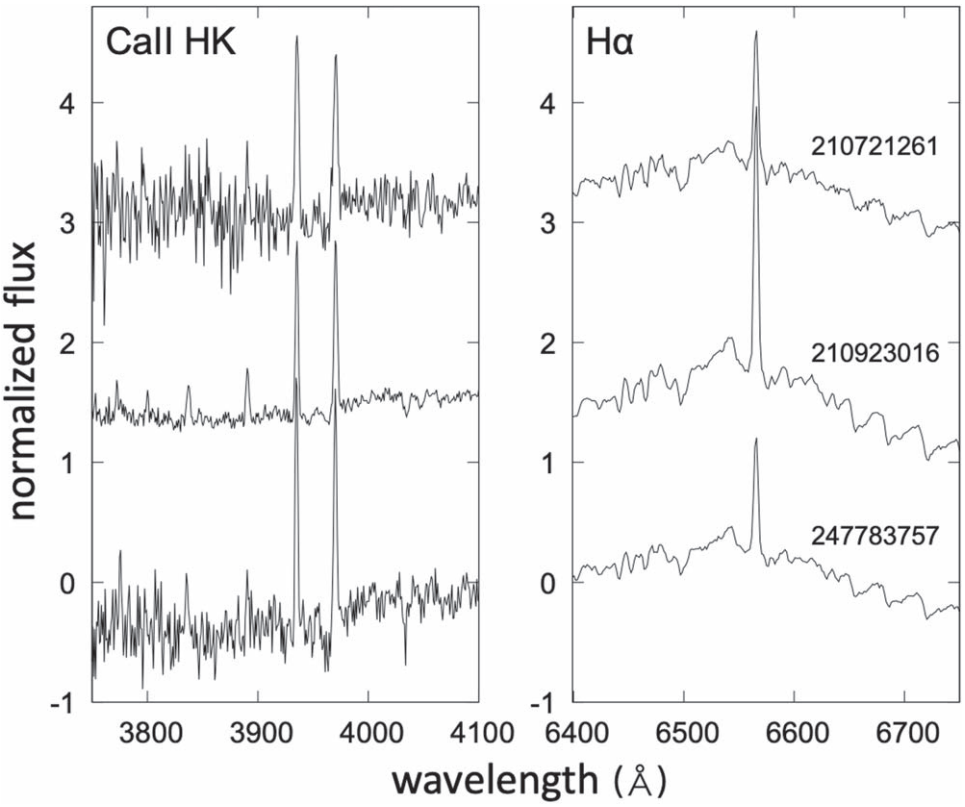

Figure 1. LAMOST low-resolution spectra for the three targets. The left and right panels show features around CaII HK and Hα emission lines, respectively.

Table 1
Stellar Properties of our Targets

	EPIC 210721261	EPIC 210923016	EPIC 247122957	EPIC 247783757
Measured Property				
Apparent B magnitude (1)	14.75 ± 0.05	15.52 ± 0.12	15.07 ± 0.04	15.55 ± 0.04
Apparent V magnitude (1)	13.31 ± 0.05	14.01 ± 0.10	13.58 ± 0.02	14.05 ± 0.05
Apparent K magnitude (1)	8.69 ± 0.02	9.22 ± 0.02	8.92 ± 0.02	9.32 ± 0.02
Parallax [mas] (2)	23.14 ± 0.05	20.90 ± 0.07	19.77 ± 0.13	20.45 ± 0.07
Astrometric Goodness of Fit: GOF_AL (2)	14.9	21.0	51.0	26.2
Astrometric Excess Noise Significance: D (2)	0.0	11.3	48.2	18.5
Renormalised Unit Weight Error: RUWE (2)	1.21	1.18	6.51	1.06
$BP - RP$ color (2)	2.39	2.54	2.47	2.53
Derived Property				
Rotation period : $P_{\rm rot}$ (3)	1.5409 ± 0.0001	1.1570 ± 0.0005	1.5457 ± 0.0002	1.8276 ± 0.0002
Effective temperature : $T_{\rm eff}$ [K] (4)	3488 ± 79	3428 ± 86	3462 ± 76	3443 ± 78
Radius : R_* [$R_\odot$] (5)	0.52 ± 0.02	0.47 ± 0.02	0.53 ± 0.02	0.47 ± 0.01
Mass : $M_\star$ [$M_\odot$] (6)	0.52 ± 0.01	0.47 ± 0.01	0.53 ± 0.01	0.47 ± 0.01
Surface gravity : log$g$ (5)(6)	4.72 ± 0.02	4.76 ± 0.03	4.71 ± 0.02	4.77 ± 0.03
Effective temperature : $T_{\rm eff}$ [K] (7)	3624 ± 45	3532 ± 45	3575 ± 45	3539 ± 45
Radius : R_* [$R_\odot$] (8)	0.43 ± 0.05	0.40 ± 0.04	0.42 ± 0.05	0.41 ± 0.05

References: (1): VizieR database (https://vizier.u-strasbg.fr/viz-bin/VizieR), (2): Gaia database (https://gea.esac.esa.int/archive), (3): this study, (4): $V - J$ vs. $T_{\rm eff}$ in Mann et al. (2015), (5): M_K vs. R_* in Mann et al. (2015), (6): M_K vs. $M_\star$ in Mann et al. (2019), (7): $BP - RP$, [Fe/H] vs. $T_{\rm eff}$ in Mann et al. (2015), and (8): $T_{\rm eff}$ vs. R_* in Mann et al. (2015).

between an astrometric model and the data depending on the presence of unresolved companions. Evans (2018) set the threshold of binarity condition to GOF_AL > 20 and D > 5. In addition, we referred the Renormalised Unit Weight Error (RUWE) statistics in the Gaia early third data release (EDR3; Gaia Collaboration et al. 2021), which is discussed in Stassun & Torres (2021). They suggest that RUWE is strongly correlated to binarity condition for $1.0 <$ RUWE < 1.4. We list the GOF_AL and D values in DR2 and RUWE values in EDR3 for our targets in Table 1.

For EPIC 210721261, the GOF_AL and D values are 14.9 and 0.0, respectively, which are significantly lower than the

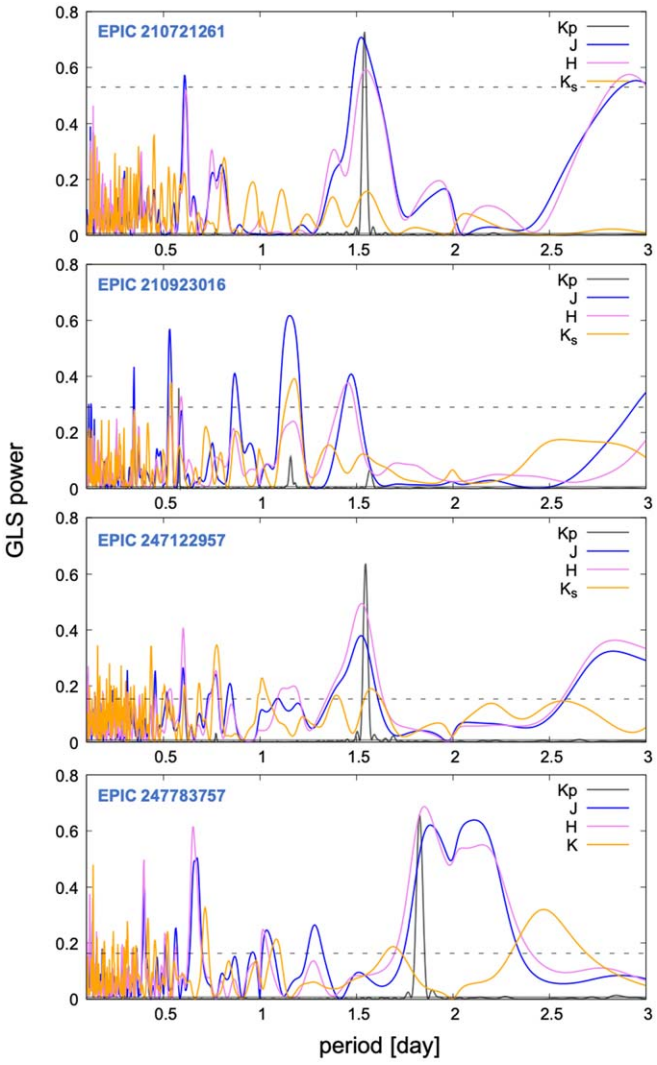

Figure 2. Generalized Lomb–Scargle periodograms for our four targets. Each solid colored line represents an observational passband. The dashed horizontal line represents 0.1% of the false alarm probability (FAP) in the *J* band. The solid horizontal line represents the 0.1% FAP in the *Kp* band.

thresholds; therefore, the possibility of a binary is low. EPIC 247122957, whose GOF_AL and D values are relatively large (51.0 and 48.2, respectively), may host a companion. For the other two targets, EPIC 210923016 and EPIC 247783757, even though their GOF_AL and D are slightly above the thresholds, we cannot confidently suggest their status as binaries. While the GOF_AL and D values were recently updated in EDR3 (Gaia Collaboration et al. 2021), we cannot directly compare them, because the thresholds in Evans (2018) were derived from the DR2 data. However, we found that the EDR3 GOF_AL values were all well under 20, except that of EPIC 247122957. With regard to RUWE, the value for EPIC 247122957 is high and deviated from the correlated range (6.51), while these for the other targets are relatively small ($\leqslant$1.2). Consequently, EPIC 210721261, EPIC 210923016, and EPIC 247783757 seem to be single stars with high probability from the aspect of astrometry.

Douglas et al. (2019) mentioned that rapid rotating early M dwarfs in Hyades with periods of $\sim$1 day are likely binaries, whereas the typical period of them is $\sim$10 days. To discuss the binarities further, we also derived stellar radii based on

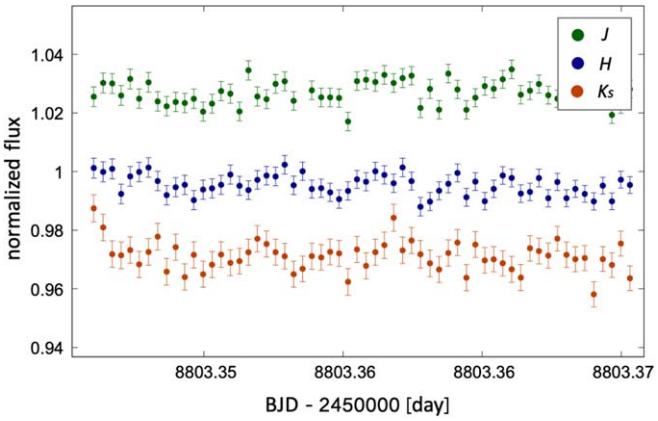

Figure 3. Example of a light-curve segment observed with IRSF. The light curve is for EPIC 210721261 and was extracted with the customized pipeline described in Fukui et al. (2011).

different photometry. We show the additional radii estimated with $T_{\rm eff}$ versus R_* relation in Mann et al. (2015) to Table 1 in italic; the $T_{\rm eff}$ is derived from $V-J$ color. There are approximately $2-\sigma$ deviations from the radii derived from M_K for all the targets. One explanation for these systematics is that our targets may be entirely binaries. If it was true, fluxes from the companions are likely not dominant because the periodograms in *Kp* band show single peaks excluding harmonics for all the targets. In Section 5, we test a dilution effect by a companion star to discuss uncertainties in the case where the targets are binaries.

2.2. Follow-up Observations, IRSF 1.4 m / SIRIUS

From November 14–26, 2019, we conducted follow-up observations with the Simultaneous Infrared Imager for Unbiased Survey (SIRIUS; Nagashima et al. 1999) on the IRSF 1.4 m telescope at the South Africa Astronomical Observatory. SIRIUS is equipped with three 1 k $\times$ 1 k HgCdTe detectors with a pixel scale of $0\farcs45$ pixel^{-1}. This enables us to take three NIR images in the *J*, *H*, and K_s bands simultaneously with the same exposure time for all bands. Setting the exposure times to 30 s with a dead time of approximately 8 s for all bands, we observed the four targets in rotation during a night. Each target was observed for approximately 30 minutes per visit, and was visited two or three times per night. The weather conditions were generally good, and observations were carried out nearly every night.

Aperture photometry for each raw-fits file has been performed using the customized pipeline described in Fukui et al. (2011). For each target, we employed two or three stars in the same frame as reference stars, and checked that their flux variations were negligible. The flux error σ for each data point was calculated as in Section 2.2 of Fukui et al. (2011). We show an example of extracted light curves for EPIC 210721261 in Figure 3. Because there are systematic errors due to the observational circumstances, we applied systematic correction to the light curves, as described in Fukui et al. (2013); here, we employed the pixel positions of the target and airmass as correction parameters. Then, we binned the light curves into 0.05 days sized bins adopting the weighted mean for each bin. The weighted mean and propagated error values in each bin were derived as $x_{\rm wm}=\sum\omega_i x_i/\sum\omega_i$ and $\sigma_{\rm wm}=1/\sqrt{\sum\omega_i}$, respectively, where the weight ω_i was given by $1/\sigma_i^2$. Note that we only consider errors in the aperture photometry, and do not

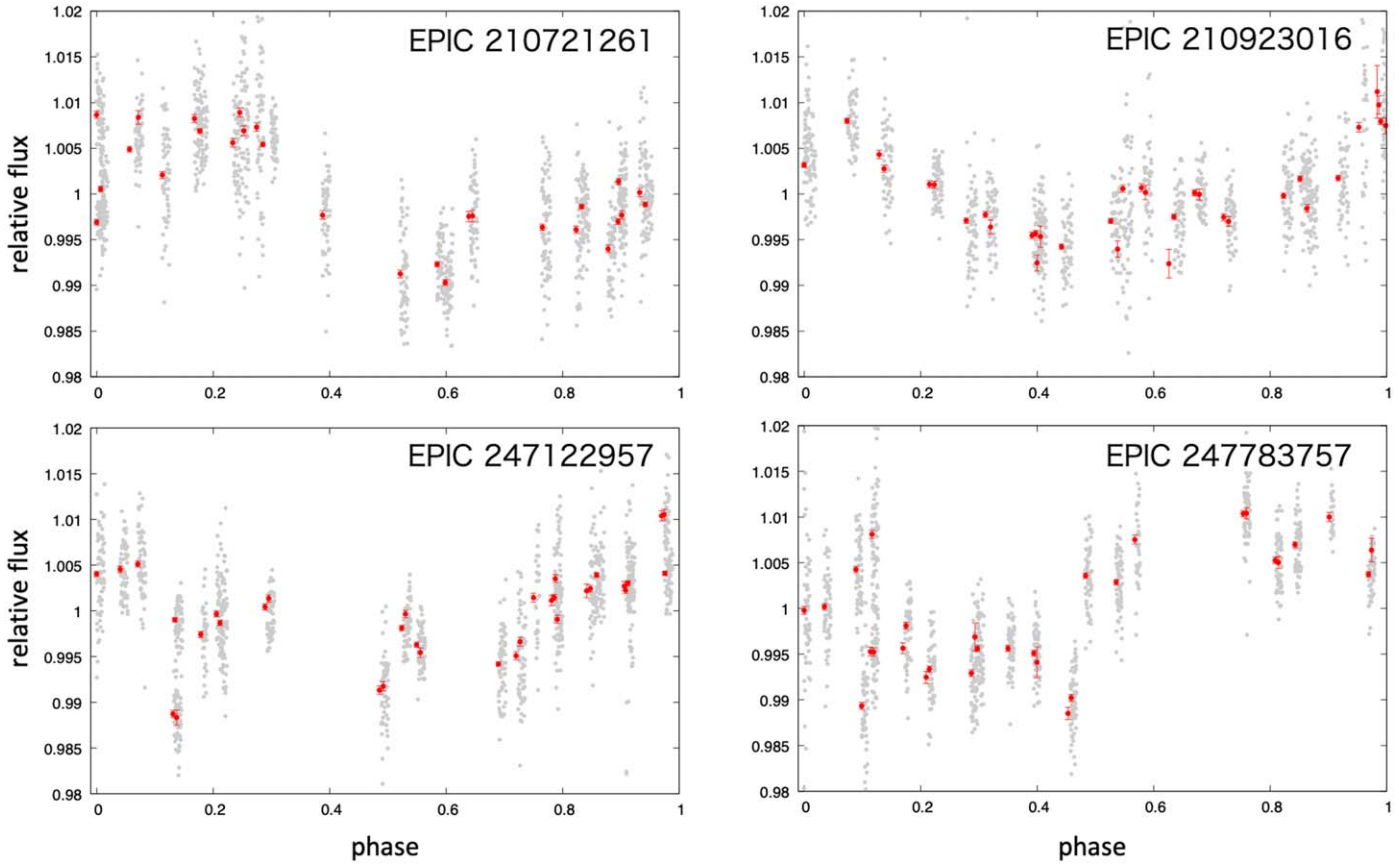

Figure 4. Folded light curves in *J*band observed with IRSF/SIRIUS. The gray and red points are unbinned and binned light curves, respectively.

take into account other factors such as instrumental noise and/or weather conditions, which may possibly lead to underestimated total errors. It is difficult to evaluate these factors directly because photometry was performed in a discrete manner over the course of two weeks. In Section 3.2, we will explain how to treat these uncertainties to estimate astrophysical signals more accurately.

We tested the reproducibility of the periodicities identified in the K2 photometry using the GLS periodograms. The results are shown in Figure 2 as solid colored solid lines for all four targets. The horizontal dashed line represents the false alarm probability of 0.1% (FAP; Zechmeister & Kürster 2009) in the *J* band. For almost targets, peaks higher than the 0.1% FAP lines were detected in the *J* and *H* bands, and the periodicities in the K_s band were not detected with sufficient significance. This is because the detector is known to be unstable, and the systematic errors were larger than the astrophysical signals for the K_s band. Overall, these periodogram results ensure the accuracies of our observational data and their reductions, although their uncertainties are likely underestimated. We show the light curves for the four targets in the *J* band observed with IRSF/SIRIUS in Figure 4. The light curves were folded with the periods detected using the GLS.

3. GP Regression to the Light Curves

We applied Gaussian process (GP) regression to quantify the behaviors of starspots in the light curves (Rasmussen & Williams 2006; Haywood et al. 2014; Grunblatt et al. 2015; Hirano et al. 2016). Detail of GP is described in Appendix A. In the following, we explain how to treat the observed light curves with GP.

3.1. Analysis of the K2 Light Curves

First, we analyzed the K2 light curves using the GP to reproduce the flux variations due to stellar rotation because these curves were sufficiently precise and collected over a long period with good cadence. We binned the light curves into 0.1 day ranges considering the computational cost and the rotation period. We employed the quasiperiodic kernel ($K_{\rm qp}$; Equation (A3)) in the GP regressions. This is because signals induced by stellar jitter show both periodicities due to stellar rotations and coherent variations due to surface activities. To optimize the hyperparameters, we used the Marcov chain Monte Carlo (MCMC) method (Foreman-Mackey et al. 2013) and added Gaussian priors based on the rotation periods in Table 2 for θ. We set the number of walkers and steps to 50 and 10^4, respectively. The initial positions of the parameters h, w, λ, and σ were set to $[10^{-3}, 10^{-1}]$, $[10^{-1}, 10^{2}]$, $[10^{-1}, 10^{2}]$, and $[10^{-4}, 10^{-2}]$, respectively with uniform distributions.

The derived hyperparameters in this analysis are listed in the upper part of Table 2. We indicate the mean with a solid line and the $1-\sigma$ and $2-\sigma$ uncertainties of the GP analyses with colored regions in Figure 5. We see quasistable, periodic variations for all targets.

3.2. Joint GP Analysis

Next, we measured the variation amplitudes h over all the passbands (Kp, J, H, and K_s) using a Bayesian approach, to

Table 2
GP Hyperparameters

	EPIC 210721261	EPIC 210923016	EPIC 247122957	EPIC 247783757
Hyperparameters (optimized in Section 3.1)				
h	0.085	0.012	0.018	0.014
θ	1.5409	1.1587	1.5475	1.8286
w	1.22	0.67	0.86	0.94
λ	51.51	22.49	24.21	25.32
σ	0.0046	0.0020	0.0013	0.0012
(estimated by the joint analysis in Section 3.2)				
h_{Kp}	$0.0802^{+0.0167}_{-0.0127}$	$0.0126^{+0.0020}_{-0.0015}$	$0.0213^{+0.0030}_{-0.0025}$	$0.0215^{+0.0037}_{-0.0030}$
σ_{Kp}	$0.0046^{+0.0002}_{-0.0002}$	$0.0020^{+0.0001}_{-0.0001}$	$0.0013^{+0.0001}_{-0.0001}$	$0.0012^{+0.0001}_{-0.0001}$
h_J	$0.0135^{+0.0082}_{-0.0048}$	$0.0052^{+0.0027}_{-0.0018}$	$0.0054^{+0.0036}_{-0.0024}$	$0.0120^{+0.0071}_{-0.0041}$
σ_J	$0.0003^{+0.0003}_{-0.0002}$	$0.0006^{+0.0005}_{-0.0003}$	$0.0016^{+0.0009}_{-0.0006}$	$0.0006^{+0.0005}_{-0.0004}$
$h_{\mathrm{sq},J}$		$0.0032^{+0.0004}_{-0.0004}$		
$\lambda_{\mathrm{sq},J}$		$0.0828^{+0.0255}_{-0.0213}$		
h_H	$0.0116^{+0.0097}_{-0.0047}$	$0.0044^{+0.0035}_{-0.0024}$	$0.0055^{+0.0032}_{-0.0021}$	$0.0089^{+0.0049}_{-0.0028}$
σ_H	$0.0005^{+0.0004}_{-0.0003}$	$0.0031^{+0.0008}_{-0.0006}$	$0.0011^{+0.0006}_{-0.0005}$	$0.0010^{+0.0005}_{-0.0004}$
$h_{\mathrm{sq},H}$		$0.0032^{+0.0005}_{-0.0004}$		
$\lambda_{\mathrm{sq},H}$		$0.0700^{+0.0370}_{-0.0273}$		
h_{K_s}	$0.0094^{+0.0104}_{-0.0064}$	$0.0058^{+0.0048}_{-0.0034}$	$0.0113^{+0.0102}_{-0.0063}$	$0.0049^{+0.0063}_{-0.0033}$
σ_{K_s}	$0.0012^{+0.0015}_{-0.0008}$	$0.0007^{+0.0018}_{-0.0005}$	$0.0010^{+0.0030}_{-0.0007}$	$0.0026^{+0.0030}_{-0.0012}$
h_{sq,K_s}		$0.0091^{+0.0010}_{-0.0011}$		
$\lambda_{\mathrm{sq},K_s}$		$0.0635^{+0.0249}_{-0.0133}$		

evaluate the wavelength dependencies of the stellar rotational activity. For the K2 light curves, we applied the quasiperiodic kernel (Equation (A3)) with θ, w, and λ set to the values determined in Section 3.1, and rederived h and σ. We ran 10^4 MCMC steps and ensured the convergence of the chains in the first 10^3 steps.

For the ground-based photometric data (J, H, and K_s), there are large systematic errors arising from instrumental and/or weather conditions. Because of the lack of accurate modeling of these systematic errors, the astrophysical signals originating from the intrinsic stellar activity could be overestimated or underestimated. Using the trial and error approach, we found that the following GP kernel, which combines the quasiperiodic and squared-exponential kernels can most effectively describe the behavior in the observed light curves:

$$K^{i,j} = K^{i,j}_{\mathrm{qp}} + K^{i}_{\mathrm{sq}}, \tag{1}$$

where the subscripts i and j indicate the passbands and the target ID, respectively. The first term $K^{i,j}_{\mathrm{qp}}$ is the quasiperiodic kernel that reproduces the intrinsic stellar flux variations. We fixed the hyperparameters in $K^{i,j}_{\mathrm{qp}}$ to the values in the Kp band except h and σ. This is because the ground-based light-curve data are sparse and it is difficult to accurately derive all the relevant parameters for the stellar jitter from the ground-based photometry alone, as seen in the treatment of the RV data in Haywood et al. (2014). Assuming that the covariance length scales and smoothing parameters are independent of the observational passband (wavelength), we allowed only h and σ, which are expected to depend on the passband, to float freely for each passband and each target. The second term K^{i}_{sq} is the squared-exponential kernel, which only accounts for the instrumental systematic errors for each passband, in which the relevant hyperparameters are shared for all four targets.

We list the mean values of each hyperparameter whose uncertainties were calculated to be in the range of 68.3% from the median of the marginalized posterior distribution in the lower part of Table 2. The hyperparameters in K^{i}_{sq} corresponding to the correlated instrumental noise are depicted with additional subscripts "sq". In Figure 6, we also show the mean and $1-\sigma$ and $2-\sigma$ uncertainties of the GP regressions to the light curves for the J, H, and K_s bands for each of the four targets. The smooth sinusoidal modulations represent the astrophysical signals modeled by $K^{i,j}_{\mathrm{qp}}$, whereas the sudden fluctuations correspond to the systematic errors modeled by K^{i}_{sq}. The latter variations act as offsets in the estimation of the signal amplitudes. In the K_s band, because the periodicities are weak for most of the targets as in Figure 2, the light curves are dominated by the sudden fluctuations due to instrumental effects. In total, the estimated amplitudes in NIR are from approximately half to one third of those in the Kp band, while there appears to be no significant differences between the NIR passbands. In particular for EPIC 210721261, the amplitude ratios for the Kp and H bands are as large as 7:1.

Generally, there is a possibility that the shape of the photometric variations changed during K2 and IRSF observations, even though we fixed the hyperparameter w and λ in this GP regression. On the other hand, our four targets show stable photometric modulations as in Figure 5. The periodogram analysis also suggests that they have single periodicities and no significant differential rotation (Reinhold et al. 2013). Davenport et al. (2015) performed light-curve analysis for a rapidly rotating ($\approx$0.6 day) M dwarf using Kepler photometry and suggested that a starspot was very stable over many years. In addition, we succeeded to detect the rotation periods from the discrete ground-based photometry, which means the

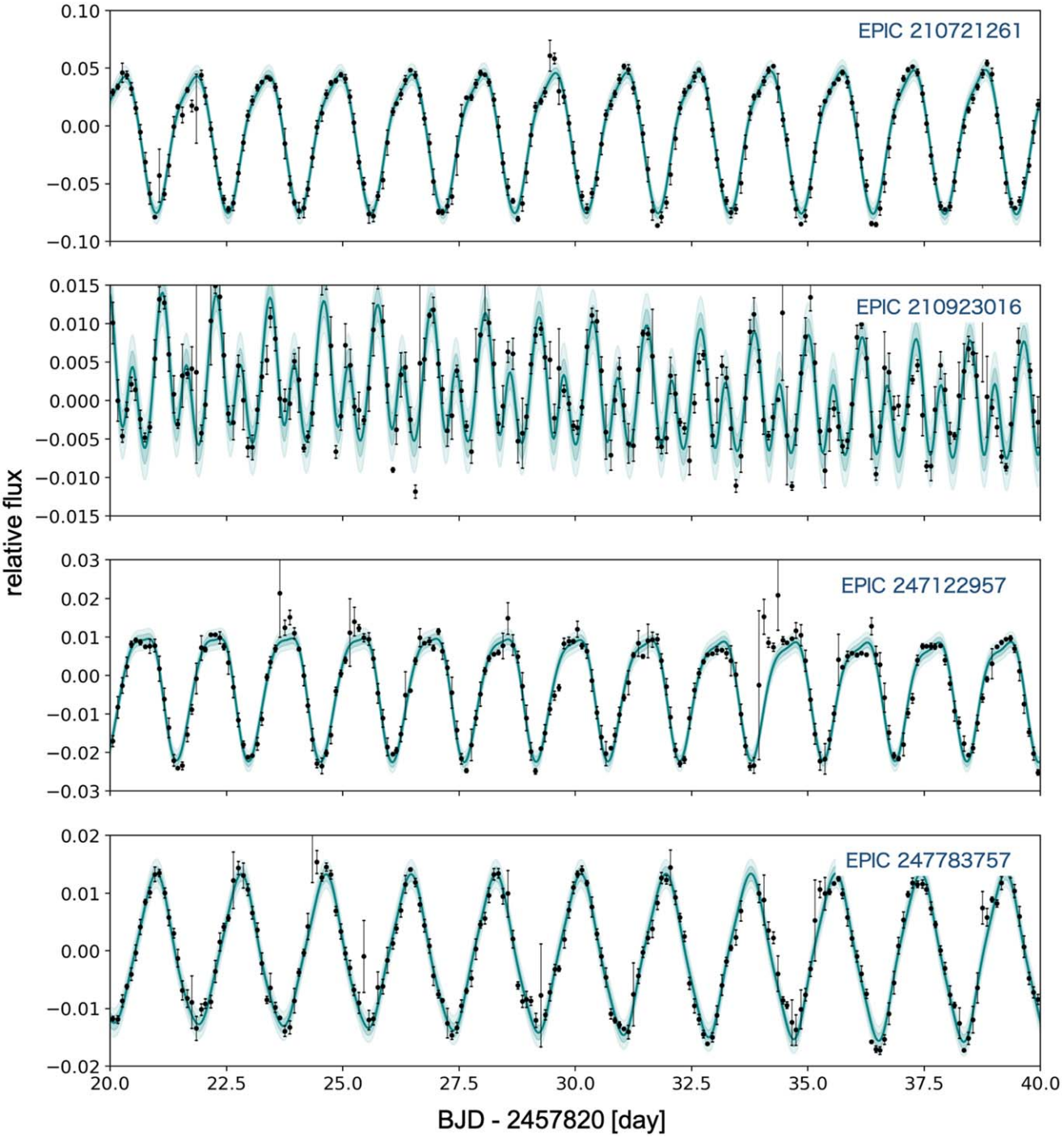

Figure 5. Examples of the K2 light curves for our targets binned with 0.1 day. The binned values and error bars were calculated as the mean and standard deviation weighted by the photon noise for each bin, respectively. The blue solid line and regions represent the result of GP analyses.

photometric variations were not complicated in the IRSF observations. Thus, we conclude that our estimations are likely consistent with the true nature of the targets.

4. Estimated Starspot Properties

4.1. Starspot Variations over 2 Years

As noted in Section 2.2, the IRSF data were observed in 2019 November, while the K2 data from Campaign 13 were observed from 2017 March 8 to May 27, meaning that these two observations were not simultaneous but were separated by approximately 2.5 yr. Within this time interval, the properties of the surface activity (jitter) may have significantly altered. Therefore, before quantitatively comparing the flux-modulation amplitudes in the K2 and IRSF data, we need to assess any long-term variations in the stellar surface activity. To do so, we focused on multiple observations of the same stars in the K2 mission: K2 observed the Hyades cluster during both Campaigns 4 and 13, spanning a time interval of approximately 2 yr. By comparing the photometric data taken during the two different campaigns, we can evaluate the long-term, temporal evolution of the surface activity. Note that our targets thast are

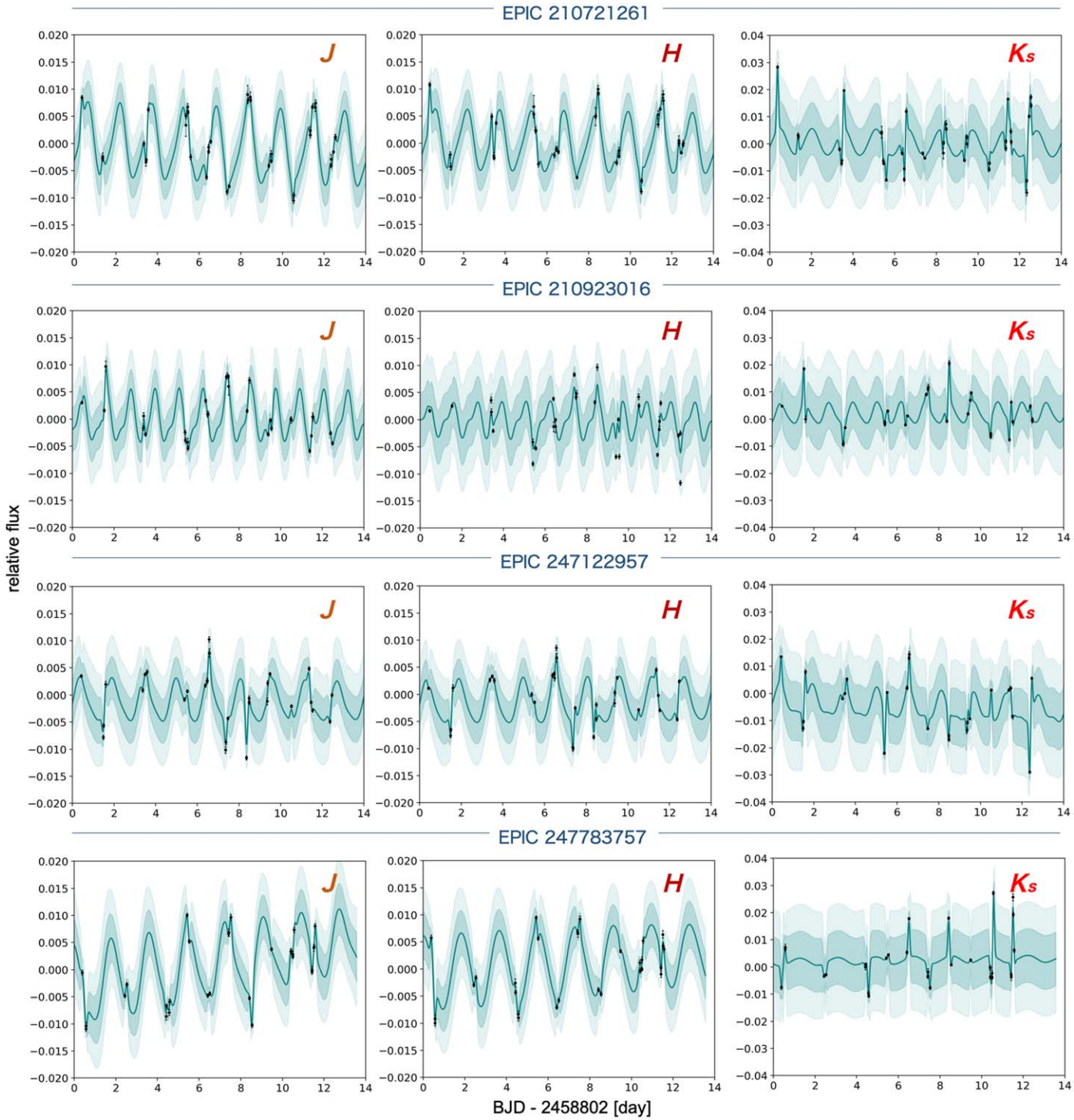

Figure 6. Light curves for all observational bands for all targets plotted with black dots. The solid blue lines and dark-colored regions represent the mean and $1-\sigma$ variance results of the GP optimization, with the light-colored regions representing the $2-\sigma$ variance results. From left to right the panels show J, H, and K_s.

rapidly rotating M dwarfs are not typical in Hyades. Thus, we use targets whose rotation periods are less than 10 days to focus on such a specific class of M dwarfs (Douglas et al. 2019).

While our targets were only observed in Campaign 13, we found that 333 EPIC targets were observed in both campaigns. Because we are focusing on cool stars in this study, we selected 95 targets with temperatures below 4000 K according the EPIC catalog (Huber et al. 2016). We normalized the light curves and removed the flux outliers as in Section 2.1. We computed the GLS periodograms to determine their rotation periods. The detection threshold in the GLS power for the K2 data was set to roughly 0.1 in reference to the periodograms in Figure 2. Consequently, we detected 19 targets whose GLS peaks are larger than 0.1 and whose periods are shorter than 10 days in either of the two campaigns. We measured the typical flux semiamplitudes of the phase-folded light curves for the 19 targets for both campaigns using GP. Here, we use the periodic kernel K_p in consideration of computational cost in the optimization with MCMC.

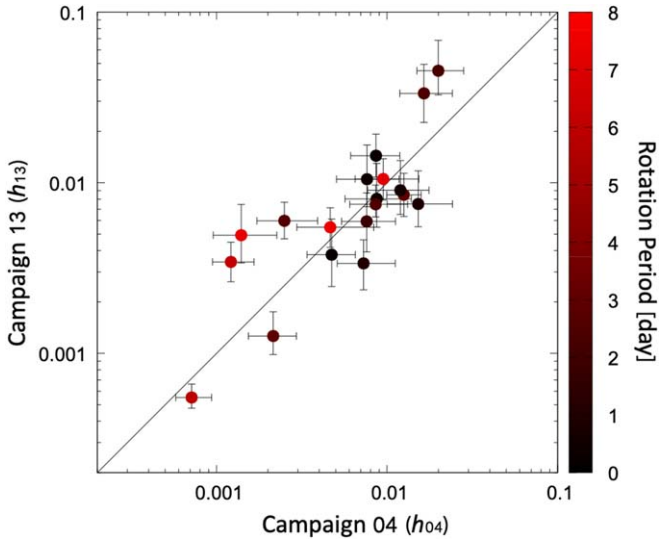

Figure 7. Comparison plot for the amplitudes of 19 M dwarfs in Hyades between Campaigns 4 and 13 on a logarithmic scale. The color for each point represents a rotation period derived using the GLS periodogram. The black solid line represents the $y = x$ line.

Examples of the folded light curves and results of the GP regressions are shown in Figure 14 in Appendix B. The properties and derived hyperparameters are listed in Table 5. One can see variations in the modulation amplitude and/or shape between the two campaigns. In Figure 7, we plot the results for all targets, showing the modulation amplitudes for Campaigns 4 and 13. The absolute variation in the amplitude is calculated as $\Delta h = |h_{13} - h_{04}|$, where h_{04} and h_{13} are the relative flux-variation amplitudes for Campaigns 4 and 13, respectively. We derived a weighted mean of Δh for 19 targets of 0.0097 ± 0.0094. The relative variation with respect to Campaign 4 ($r \equiv \Delta h/h_{04}$) was determined to be $38\% \pm 71\%$; therefore, that the variation in the modulation amplitudes at a timescale of $\sim$2 yr (between Campaigns 4 and 13) is likely lower than 100% of the original flux modulation.

4.2. Estimations of Starspot Sizes and the Temperatures

To understand the behaviors and properties of starspots more quantitatively, we estimated their sizes and temperatures from the amplitudes measured in the multicolor photometry. In general, it is difficult to solve degeneracies on surface properties (e.g., starspot latitude, number of starspots, and inclination) from shape of light curves as described in (Luger et al. 2021). Therefore, we employed a very simple toy model, which considers only the maximum projected size and temperature (see Figure 8), because we focus only on "relative" variations between different passbands, which are independent of the geometric structures of the photosphere and starspots. In the fiducial case, because the variation amplitudes are determined from the appearance and disappearance of the starspots, we ignore the effect of the limb darkening in this analysis. The modeled semiamplitude $h_{\rm model}$ is calculated as follows

$$h_{\rm model} = (1 - f_{\rm spot}/f_{\rm phot}) \times S/2, \quad (2)$$

where $f_{\rm spot}$ and $f_{\rm phot}$ are the fluxes of the starspot and the photsphere, respectively, and S represents the projected size of the starspot relative to the stellar disk, i.e., $S = 1.0$, meaning that a starspot covers a stellar hemisphere. We used the PHOENIX atmosphere model (Allard et al. 2013) to derive the photometric fluxes from the temperatures of the spot ($T_{\rm spot}$) and photosphere ($T_{\rm phot}$). We generated the model spectra using a step of 100 K for the effective temperature from 1600–4000 K, and interpolated the intermediate values using a the third-order spline curve with the metallicity set to 0.0. We derived the photometric flux for each observational passband as the photon count per unit area by multiplying the model spectra by the response function for each passband and integrating with respect to the wavelength (e.g., Fukugita et al. 1995). The response functions are taken from the websites for each instrument.[12,13] We used the measured amplitudes h in Section 3.2 for the observed values. Because there are systematic uncertainties due to the different observational windows for the K2 and IRSF runs, as in Section 4.1, we added the relative variation r to the errors in the K2 data in quadrature such that $((h_{Kp} \times r)^2 + \eta_{Kp}^2)^{1/2}$, where η_{Kp} is the internal error for h_{Kp}. The photospheric temperature $T_{\rm phot}$ was set to the stellar effective temperature in Table 1. For each target, we fitted the observed flux-modulation amplitude for each band by optimizing the projected size S and the temperature $T_{\rm spot}$ of the starspot. We ran 10^4 MCMC steps with uniform priors in the range of [0.0, 1.0] and [1600, $T_{\rm phot}$) for S and $T_{\rm spot}$, respectively, by maximizing the logarithmic likelihood $\log \mathcal{L}_h$ such that

$$\log \mathcal{L}_h \propto -\frac{1}{2}\sum_i \frac{(h_{{\rm model},i} - h_i)^2}{\eta_i^2}, \quad (3)$$

where i is an index indicating the observational passband.

The derived medians and 68.3% uncertainties of the posterior distributions are given in Table 3 and Figure 9. We show the fitting results of the signal variations in Figure 10. The observed values are plotted with the yellow stars, and the posterior distributions of the modeled amplitudes $h_{\rm model}$ are represented by orange hexagons which are spread horizontally to easily discern each passband. Only in the case of EPIC 210721261 does the posterior distribution in the *Kp* band deviate significantly from the observed value. The other targets show good agreement for all passbands. The uncertainties with respect to the estimated sizes and temperatures are relatively large because the statistical error in h derived from the photometry is large. For all targets, we can see elongated posteriors in Figure 9 as a result of the degeneracy in the starspot size and temperature.

To take into account the case that the photospheric temperatures were misdetermined due to their young active natures, we performed additional analyses assuming ± 200 K differences on the $T_{\rm phot}$. The results are also listed in Table 3; there are no significant deviations from the fiducial values. Therefore, our conclusions on the $T_{\rm spot}$ are not likely severely affected by the uncertainties in the photospheric temperature. We note that our modeling cannot solve degeneracies about the starspot size if large polar spots and/or axis-symmetrically distributed spots exist on the photosphere, because they do not appear in the one-dimensional light curves.

[12] https://keplerscience.arc.nasa.gov/data/kepler_response_hires1.txt
[13] http://www-ir.u.phys.nagoya-u.ac.jp/~irsf/sirius/tech/index.html

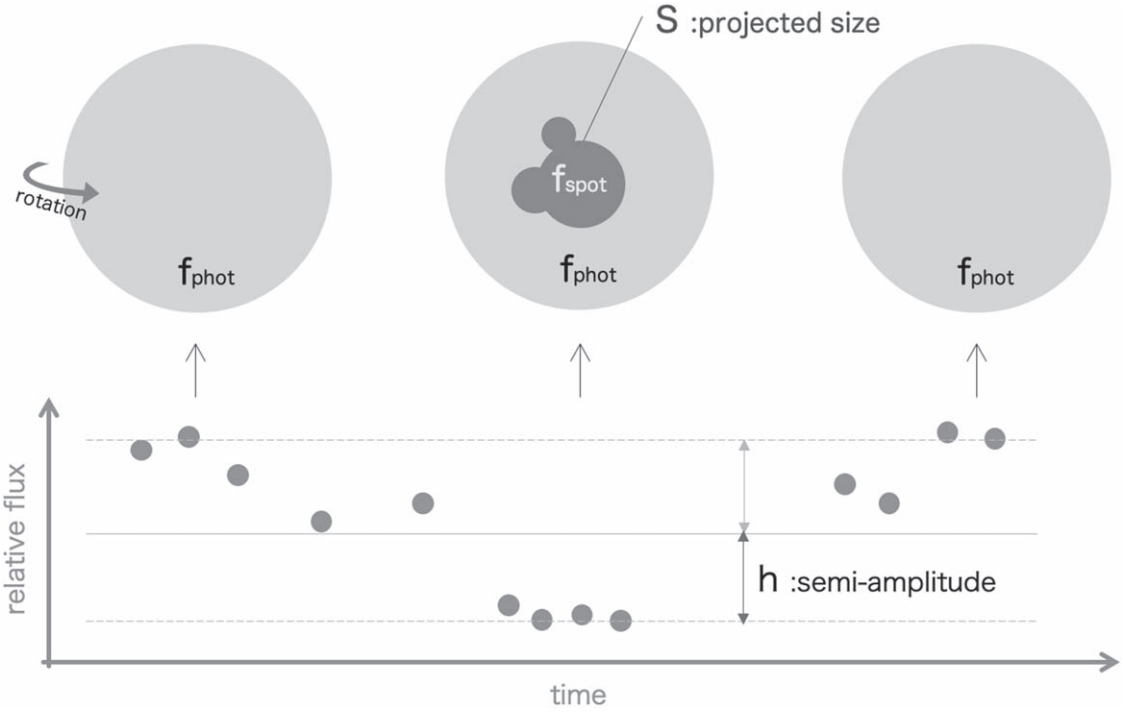

Figure 8. Illustration of the simple model for the estimation of spot size and temperature (upper picture) and corresponding image of flux variation (lower picture), where $f_{\rm spot}$ and $f_{\rm phot}$ are fluxes on the starspot and the photosphere regions, respectively; h is semiamplitude of the relative flux variation. The projected size of the starspot S is defined to be 1.0 when covering a stellar hemisphere. Here, we do not consider the shape, surface distribution, or rotation axis.

Table 3
Derived Starspot Sizes and Temperatures

EPIC ID	size [%]	temperature [K]	$T_{\rm spot}/T_{\rm phot}$	size [%]	$T_{\rm spot}/T_{\rm phot}$ +200 K	size[%]	$T_{\rm spot}/T_{\rm phot}$ −200 K
210721261	18^{+36}_{-12}	3269^{+153}_{-652}	$0.94^{+0.04}_{-0.18}$	13^{+49}_{-9}	$0.94^{+0.06}_{-0.22}$	17^{+35}_{-11}	$0.93^{+0.05}_{-0.17}$
210923016	8^{+34}_{-6}	3261^{+137}_{-612}	$0.95^{+0.04}_{-0.18}$	5^{+36}_{-3}	$0.93^{+0.06}_{-0.22}$	9^{+36}_{-6}	$0.96^{+0.04}_{-0.17}$
247122957	14^{+35}_{-10}	3332^{+97}_{-463}	$0.96^{+0.03}_{-0.13}$	8^{+41}_{-5}	$0.96^{+0.03}_{-0.20}$	11^{+38}_{-8}	$0.95^{+0.04}_{-0.14}$
247783757	10^{+34}_{-6}	3189^{+202}_{-706}	$0.93^{+0.06}_{-0.21}$	6^{+36}_{-4}	$0.91^{+0.08}_{-0.23}$	10^{+34}_{-7}	$0.93^{+0.05}_{-0.19}$

5. Discussion & Summary

5.1. Wavelength Dependence of RV Jitter

We estimated the amplitudes of the flux modulations due to stellar surface activity for the four targets in the Hyades cluster, and constrained the starspot sizes and temperatures using a simple toy model. For EPIC 210721261, the model in the *Kp* band deviates from the observed amplitude, likely as a result of the particularly enhanced activity of the star when the K2 observations were made. EPIC 210721261 is the only target, whose the possibility of binarity is significantly low based on the works of Evans (2018) with the Gaia DR2 data; for the other targets, it is possible that the starspot contrasts versus the wavelength are diluted by the presence of a companion. However, the Gaia EDR3 data (Gaia Collaboration et al. 2021) suggest binarity only for EPIC 247122957. In addition, because we assumed only cool starspots as elements of the surface activity, as opposed to plages, flares, or hot starspots, our model may differ significantly from the true stellar photosphere. In either case, the reduction rate of the photometric variations between the *Kp* and *H* bands ($1 - h_H/h_{Kp}$) is approximately 0.6 at maximum.

To predict RV jitter in the observing bandpasses, we approximated the maximum amplitudes as $h \times V_{\rm eq}$ (Aigrain et al. 2012) when the starspot is on the equator and the rotational inclination is 90°, where $V_{\rm eq}$ is the equatorial rotational velocity; these approximations are listed in Table 4. Consequently, we found that RV jitter in the NIR is significantly suppressed compared to jitter in visible wavelengths and that there is no significant difference between the *J*, *H*, and K_s passbands.

5.2. Comparison with Previous Studies of the Starspot Property

Frasca et al. (2009) measured the starspot properties of six cool stars whose photometric variations are typically $\Delta{\rm mag}_H \approx 0.1$ (∼10% in relative flux) in the pre-main-sequence phase (∼10 Myr) using the simultaneous multicolor photometry in the *R*, *I*, *J*, and *H* bands. They derived the starspot size *S* and the temperature ratio between the starspot and the photosphere $T_{\rm spot}/T_{\rm phot}$ to be 5%–10% and 0.70–0.90, respectively. Our estimations are 8%–18% and 0.93–0.96, respectively, for 650 Myr cool stars. Even though the sizes depend on the selection biases of the targets, these results may suggest that the temperature difference between starspot and the photosphere becomes smaller with stellar age.

In some previous studies, the starspot to photosphere temperature ratio $T_{\rm spot}/T_{\rm phot}$ was estimated to be approximately

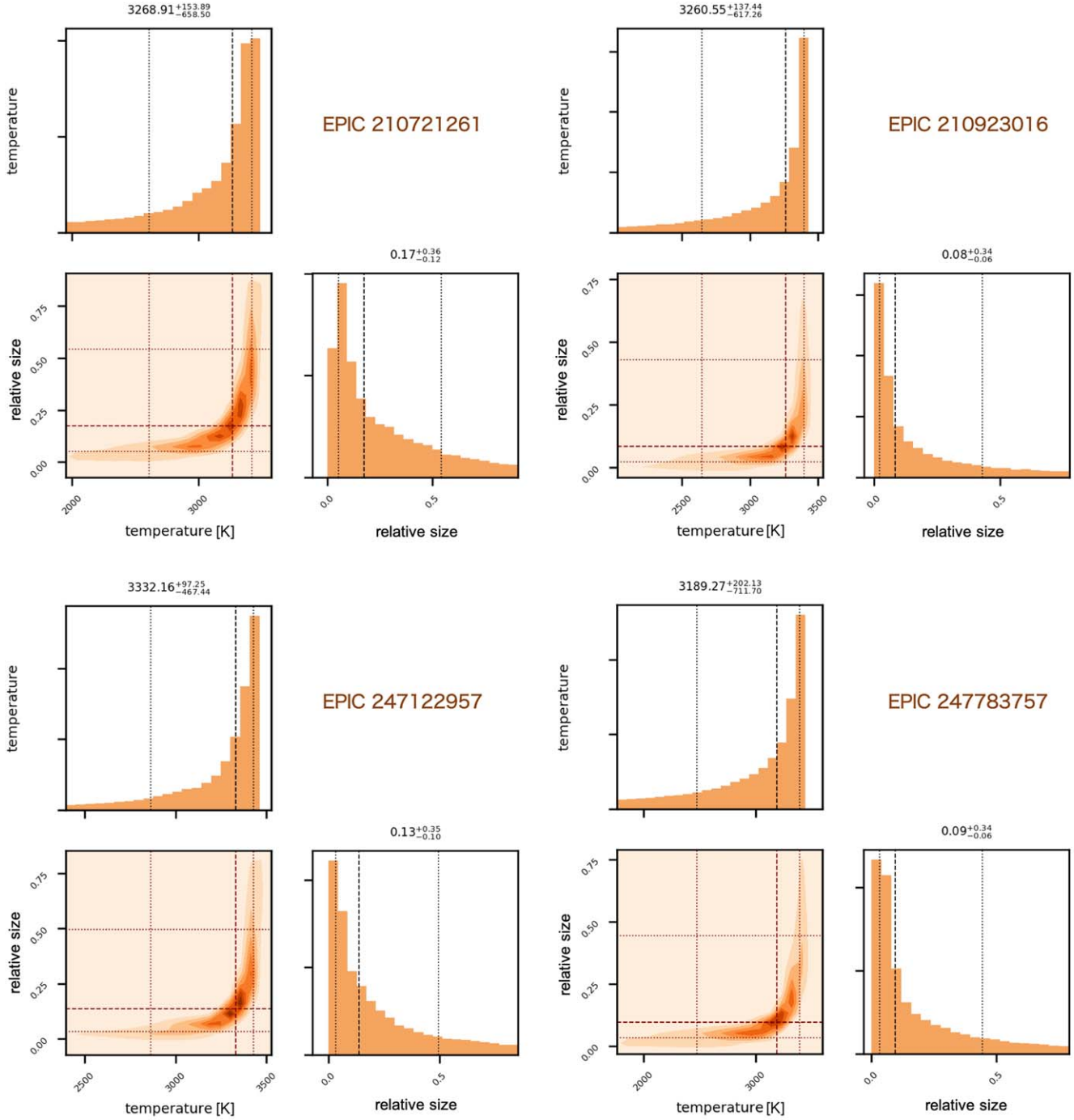

Figure 9. Posterior distributions of MCMC sampling for estimations of the starspot temperatures and relative sizes.

0.8 for G- and K-type stars according to line-depth ratio measurements, which are currently believed to be the most reliable method to characterize the properties of starspots (e.g., Catalano et al. 2002; Frasca et al. 2008). In addition, O'Neal et al. (1996) and Frasca et al. (2008) suggested that $\Delta T = T_{\rm spot} - T_{\rm phot}$ increases with surface gravity of the star, which may be explained by the balance of magnetic and gas pressures in flux tubes. However, our estimation appears to be systematically inconsistent with their theory considering the high surface gravity of our targets in Table 1. In addition, from results found in different models, Berdyugina (2005) and Strassmeier (2009) showed that ΔT gets smaller for cooler stars by as much as 200 K. We plot the previous ΔT estimations from Berdyugina (2005) and Frasca et al. (2008, 2009) in the left panel of Figure 11. Our results with the red points seem to follow this trend, although the derived values of ΔT are estimated to be slightly small. The 3D radiative MHD simulations of starspots performed in Panja et al. (2020) also explained this trend with the dependence of opacity on temperature which is largely governed with H^- ions. Note that previous estimations of M dwarfs were derived using single-band light-curve modeling (e.g., Rodono et al. 1986), which includes degeneracy between the starspot temperature and size. In addition, the samples used include large systematic

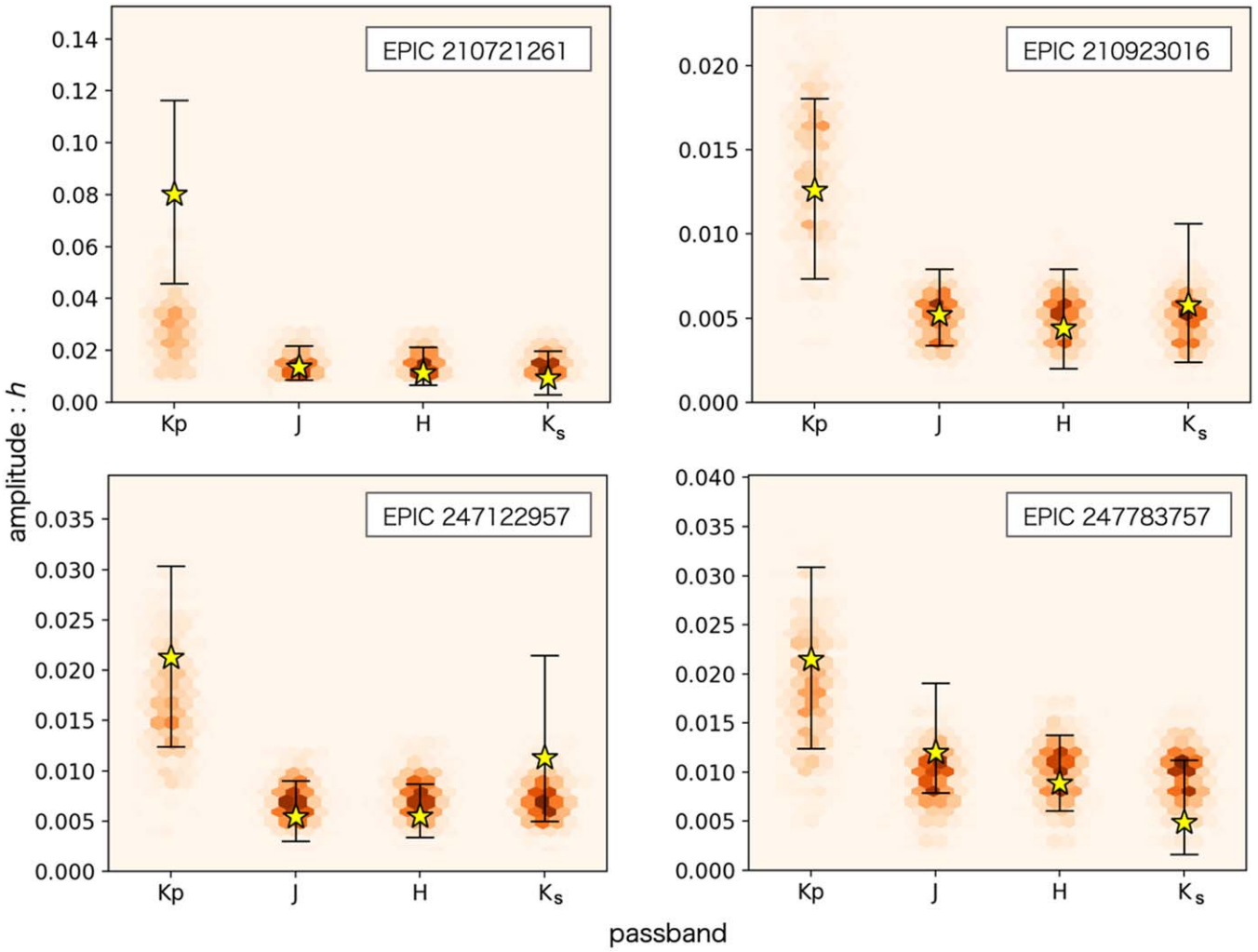

Figure 10. Variation amplitude for each observational passband for our targets. The yellow stars represent the measured values in Section 3.2. The orange hexagons represent the model values derived from the posterior distribution of the MCMC sampling. The error bars of the observed values for *Kp* band were enlarged by *r*, originating from the uncertainty in the spot evolution over the two years as in Section 4.1.

Table 4
Estimated RV Jitter from the Photometry

EPIC ID	Kp(ms^{-1})	J(ms^{-1})	H(ms^{-1})	K_s(ms^{-1})
210721261	1370	230	198	160
210923016	259	106	91	119
247122957	370	94	95	196
247783757	280	156	116	64

uncertainties associated with the stellar evolution stage. In the right panel of Figure 11, we also show ΔT with respect to the Rossby number which is related to the magnetic activity in stellar dynamo (Kim & Demarque 1996) and is approximated as $Ro = v/(2\Omega L)$; v, Ω, and L are surface velocity, angular velocity, and typical length, respectively. Here, we use the square root of the spot area for L, and macroturbulence velocity for v, which is calculated assuming that v linearly depends on the photospheric temperature in the range of $3000 < T_{\rm phot} < 4500$ Kand $1 < v < 2$ kms^{-1}, respectively. ΔT for our targets are significantly lower than the previous estimations for pre-main-sequence stars and the systematic trend with *Ro* is unclear. In any case, additional investigations are required for further relevant discussions.

5.3. Model Uncertainty

In Figure 12, we plot the theoretical semiamplitude (h_{Kp} and h_H) with setting S to 1.0 in the left panel and the corresponding contrast (h_{Kp}/h_H) in the right panel as a function of the temperature ratio $T_{\rm spot}/T_{\rm phot}$ in cases where the photospheric temperature is either 4000 K or 3000 K with the PHOENIX model spectra. The gray lines represent the values for EPIC 210923016 (3428 K) and EPIC 247783757 (3443 K), whose contrasts are relatively small in our targets. This contrast figure suggests that as the starspot temperature asymptotically approaches the surface temperature, the contrasts between the starspot and the photosphere for the optical and NIR passbands become larger. Therefore, the starspots need to be hot at the same level as the photosphere to explain our observational results. Nevertheless, the observed contrasts are still larger than the theoretical model expectations for EPIC 210721261, EPIC 210923016, and EPIC 247122957. Note that contrasts for EPIC 210721261 and EPIC 247122957 are beyond the range of the figure. This discrepancy is preferable for the detection of true planetary signals via NIR observations, albeit the reason for this may stem from the incompleteness of the models.

We also estimated the amplitude variation ratio between the *H* and *Kp* bands due to an unresolved cool companion. We

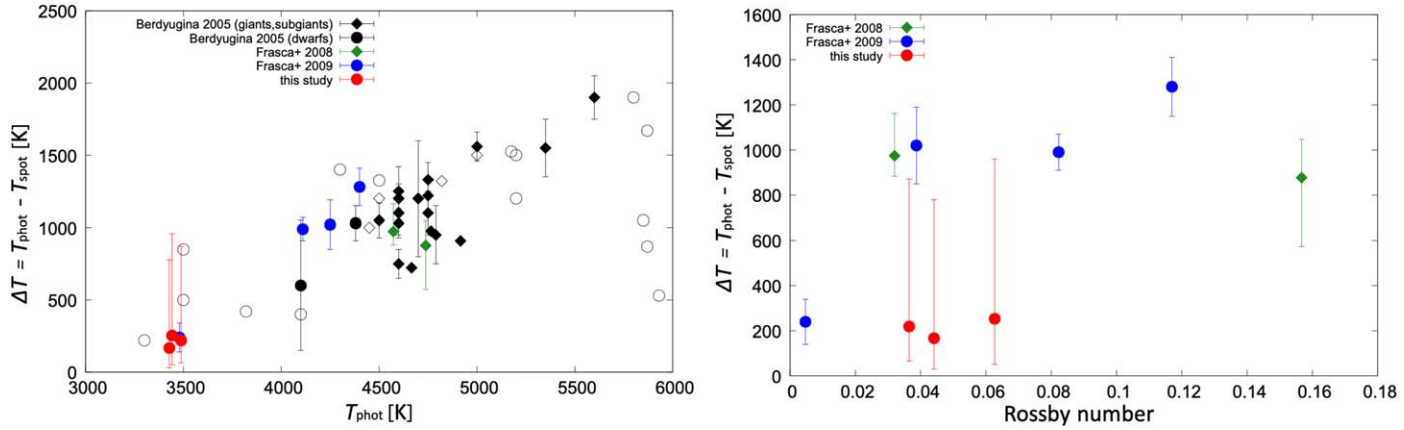

Figure 11. Left: temperature differences between the starspot and the photospere with respect to the photospheric temperature. The black, green, blue, and red points indicate values from Berdyugina (2005) and Frasca et al. (2008, 2009) and this study, respectively. The diamond and circular symbols represent giants/subgiants and dwarfs, respectively. We show the data points without errors with open circles from Berdyugina (2005). We omit EPIC 247122957 because of the high probability of binarity. Right: the temperature differences against the Rossby number. The same symbols and colors are used as in the left panel.

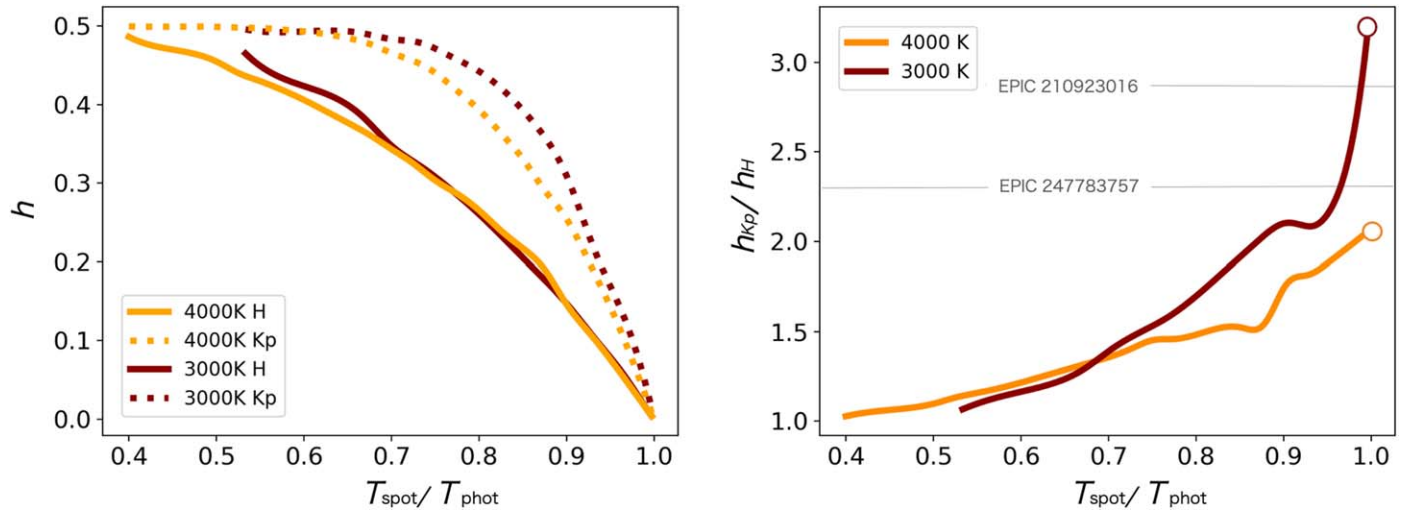

Figure 12. Left: theoretical relationships between the relative starspot temperature and the relative flux semiamplitude, h, when the projected size S is 1.0 calculated with the PHOENIX model spectra. The solid and the dotted lines to H band and Kp band, and the orange and the red lines to stellar photospheric temperatures of 4000 K and 3000 K, respectively. Right: theoretical relationship between the relative starspot temperature and the ratio of the variation of the H band with respect to the Kp band. The line color relationship is the same as the left figure. The gray horizontal lines indicate the measured values for EPIC 210923016 and EPIC 247783757 as a reference; note that the values for the other two targets are beyond the figure frame.

calculated fluxes ($f_{\rm host}$, $f_{\rm comp}$) with the PHOENIX model spectra and derived the radii ($r_{\rm host}$, $r_{\rm comp}$) with a temperature-radius relationship in Mann et al. (2015) for the host and the companion, respectively. The signal dilution d due to the companion is derived as,

$$d = f_{\rm host} / \left\{ f_{\rm host} + f_{\rm comp} \left(\frac{r_{\rm comp}}{r_{\rm host}} \right)^2 \right\}.$$

The contrast between the bands is estimated as d_{Kp}/d_H and shown in Figure 13. The maximum variation is approximately 15%, which is significantly smaller than the variation due to the starspot. For example, the starspot temperature would be 3330^{+100}_{-492} K for EPIC 247122957, even after the consideration of the 15% amplitude decrease in Kp band. Therefore, our conclusions are not affected seriously even though the targets are binaries.

5.4. Advantage of This Study

Previous studies on starspots were performed for bright targets whose high-resolution spectra are available (Catalano et al. 2002) or whose photometric variations are sufficiently large (∼10%), such as pre-main-sequence stars (Frasca et al. 2009). Our approach, which combines space telescope and ground-based photometry, is applicable to a larger sample of targets with relatively small variations (∼1%). Even though the simple modeling to the multicolor photometry still includes degeneracies on geometry of the starspots, it is useful for investigating the macrotemperature structure on the stellar surface. Because the K2 and TESS missions collected and are collecting many light curves of young stars belonging to various stellar clusters, a similar approach to that presented here could reveal the statistical properties of stellar activities at different ages.

Finally, we suggest that the mitigation of RV jitter in the NIR could be more significant than expected from theoretical

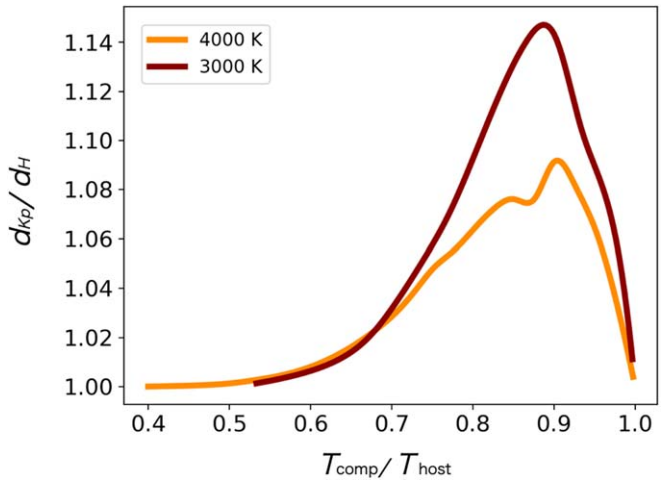

Figure 13. Theoretical relationship between the relative companion temperature and the ratio of the variation of the *H* band with respect to the *Kp* band. The line color relationship is the same as Figure 12.

models, even though further observations with a larger sample are required to corroborate this possibility. To take advantage of NIR spectroscopy in Doppler observations, new NIR high-resolution spectrographs have been developed over the last decade, such as CARMENES at the Calar Alto 3.5 m telescope (Quirrenbach et al. 2016), the Habitable–Zone Planet Finder (Mahadevan et al. 2014) on the Hobby Eberly Telescope, SPIRou on the CFHT 3.58 m telescope (Artigau et al. 2014), and the InfraRed Doppler spectrograph on the Subaru 8.2 m (Tamura et al. 2012; Kotani et al. 2014, 2018). Our results support the effectiveness of these NIR observations. In the near future, more accurate estimations of the properties of planetary systems around young stars will be possible by combining photometric and spectroscopic NIR observations, which will offer important clues understanding the formation and evolution processes of exoplanetary systems.

This paper is based on data collected at IRSF. We thank Kumiko Morihana and the other members of IRSF team for support of the observation. This work was supported by Japan Society for Promotion of Science (JSPS) KAKENHI grant Nos. JP19J21733 and 17H04574. This work has made use of data from the European Space Agency (ESA) mission Gaia (https://www.cosmos.esa.int/gaia), processed by the Gaia Data Processing and Analysis Consortium (DPAC, https://www.cosmos.esa.int/web/gaia/dpac/consortium). Funding for the DPAC has been provided by national institutions, in particular the institutions participating in the Gaia Multilateral Agreement.

Appendix A
GP Regression

GP is a nonparametric regression technique to analyze observed data having n points. It models an $n \times n$ covariance matrix that expresses the correlation between the data points using kernel functions. In this study, we used the "*squared-exponential*" kernel, "*periodic*" kernel, and "*quasiperiodic*" kernel, as used in, e.g., Grunblatt et al. (2015) as follows:

$$K_{\rm sq} = h^2 \exp\left[-\left(\frac{t_i - t_j}{\lambda}\right)^2\right], \tag{A1}$$

$$K_p = h^2 \exp\left[-\frac{\sin^2\{\pi(t_i - t_j)/\theta\}}{2w^2}\right], \tag{A2}$$

$$K_{\rm qp} = h^2 \exp\left[-\frac{\sin^2\{\pi(t_i - t_j)/\theta\}}{2w^2} - \left(\frac{t_i - t_j}{\lambda}\right)^2\right], \tag{A3}$$

where t is the data point of time, h is the covariance amplitude, λ is the covariance length scale, θ is the period of the variation, and w is the smoothing parameter of the periodicity for each kernel. The squared-exponential kernel expressed by Equation (A1) reproduces the continuous data points in the observed signals, and is often used for estimations and/or corrections to systematic errors. Equation (A2) is the periodic kernel, which is used to flexibly model periodic signals including nonsinusoidal variations. The quasiperiodic kernel consisting of periodic and squared-exponential components (Equation (A3)) is often used to model quasiperiodic signals, including coherent modes such as stellar jitter.

We optimized the hyperparameters of the kernels by maximizing the likelihood $\mathcal{L}$. Under the assumption that $\mathcal{L}$ follows an n-dimensional Gaussian distribution, the logarithmic likelihood is described with observed data points y as

$$\log \mathcal{L} = -\frac{n}{2}\log(2\pi) - \frac{1}{2}\log(|K + \sigma^2 I|) - \frac{1}{2}\underline{y}^T \cdot (K + \sigma^2 I)^{-1} \cdot \underline{y},$$

where I represents the identity matrix, $\underline{y}$ is the vector of the residuals of y from the mean, and σ is white noise, which represents the statistical uncertainty of each data point. In the maximization, we optimized the white noise component by including the internal uncertainty of the observed data point ($\sigma_{\rm internal}$; i.e., photon noise) as $\sigma = (\sigma^2_{\rm internal} + \sigma^2_{\rm white})^{1/2}$. We performed the MCMC analysis provided by the Python package `emcee` (Foreman-Mackey et al. 2013) to maximize the likelihood.

Appendix B
Summary of the 19 Targets in K2

Here, we summarize the properties of the 19 targets in Section 4.1. The effective temperature derived in Huber et al. (2016), the rotation period with GLS (Zechmeister & Kürster 2009), and the hyperparameters of the periodic kernel in GP are listed in Table 5. The results of the GP analyses for all the targets in both Campaign 4 and 13 are shown in Figure 14.

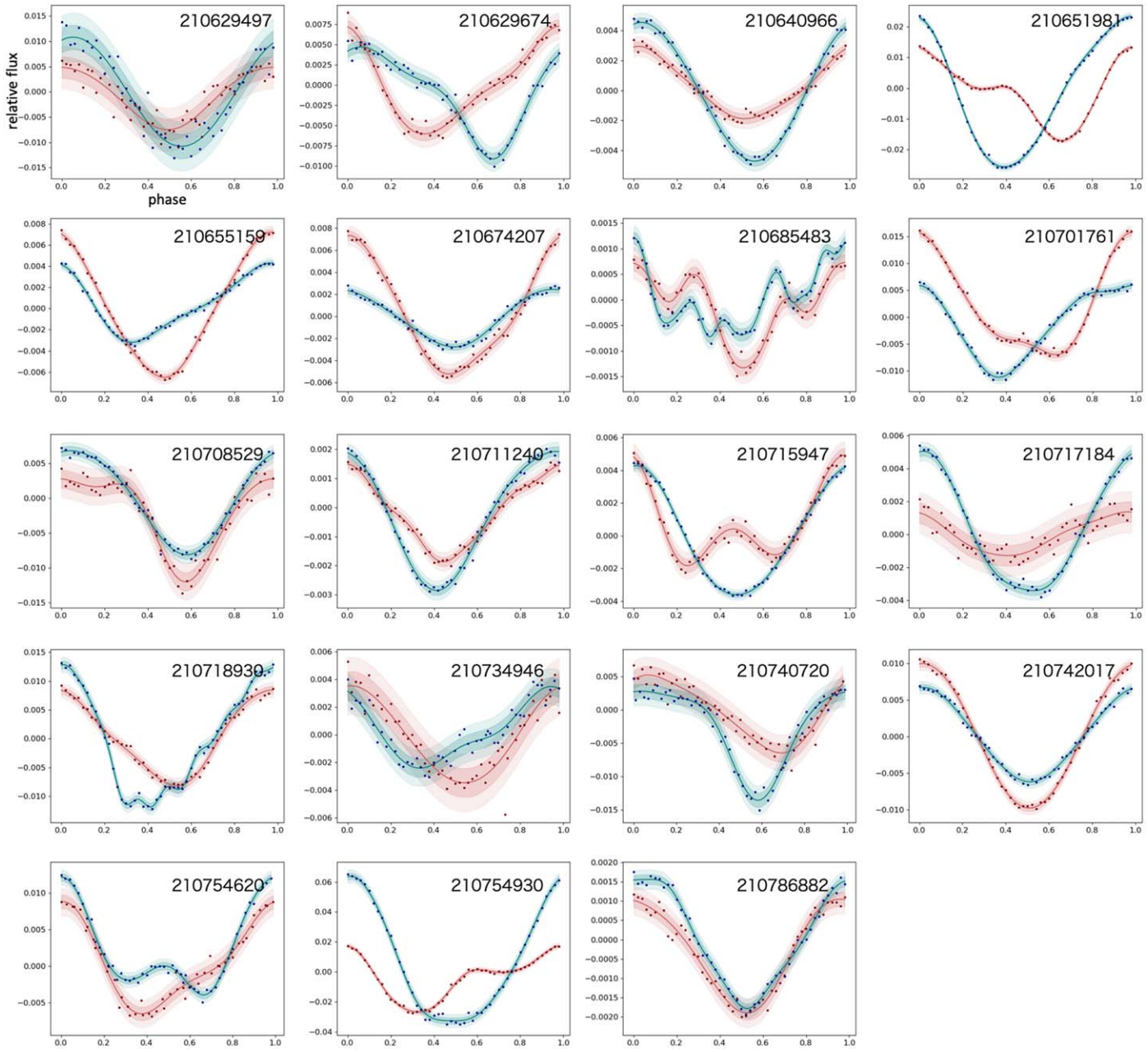

Figure 14. Examples of the phase-folded light curve for 19 Hyades M dwarfs. The red and blue data are in Campaign 4 and 13, respectively. The solid lines and colored regions represent the means and variances derived using GP with a periodic kernel.

Table 5
Derived Properties of 19 Targets

EPIC ID	Temperature [K] (1)	Period [day] (2)	h_{04}	w_{04}	σ_{04}	h_{13}	w_{13}	σ_{13}
210629497	3567	0.27	$0.0086^{+0.0032}_{-0.0024}$	$2.38^{+0.43}_{-0.59}$	$0.0020^{+0.0001}_{-0.0001}$	$0.0143^{+0.0048}_{-0.0036}$	$2.55^{+0.32}_{-0.52}$	$0.0023^{+0.0001}_{-0.0001}$
210629674	3523	0.40	$0.0086^{+0.0051}_{-0.0030}$	$1.82^{+0.56}_{-0.44}$	$0.0007^{+0.0000}_{-0.0000}$	$0.0080^{+0.0049}_{-0.0025}$	$1.58^{+0.47}_{-0.34}$	$0.0006^{+0.0000}_{-0.0000}$
210640966	3387	2.55	$0.0024^{+0.0014}_{-0.0007}$	$1.57^{+0.58}_{-0.40}$	$0.0003^{+0.0000}_{-0.0000}$	$0.0059^{+0.0017}_{-0.0012}$	$2.70^{+0.21}_{-0.38}$	$0.0003^{+0.0000}_{-0.0000}$
210651981	3712	2.44	$0.0164^{+0.0076}_{-0.0045}$	$1.42^{+0.24}_{-0.19}$	$0.0004^{+0.0000}_{-0.0000}$	$0.0333^{+0.0160}_{-0.0107}$	$2.15^{+0.43}_{-0.43}$	$0.0005^{+0.0000}_{-0.0000}$
210655159	3805	1.83	$0.0075^{+0.0036}_{-0.0021}$	$1.87^{+0.49}_{-0.36}$	$0.0002^{+0.0000}_{-0.0000}$	$0.0059^{+0.0027}_{-0.0020}$	$2.21^{+0.48}_{-0.49}$	$0.0002^{+0.0000}_{-0.0000}$
210674207	3071	1.05	$0.0072^{+0.0038}_{-0.0021}$	$1.76^{+0.42}_{-0.32}$	$0.0004^{+0.0000}_{-0.0000}$	$0.0033^{+0.0012}_{-0.0010}$	$2.43^{+0.40}_{-0.80}$	$0.0002^{+0.0000}_{-0.0000}$
210685483	3800	5.86	$0.0007^{+0.0002}_{-0.0001}$	$0.63^{+0.10}_{-0.08}$	$0.0001^{+0.0000}_{-0.0000}$	$0.0005^{+0.0001}_{-0.0000}$	$0.34^{+0.08}_{-0.04}$	$0.0001^{+0.0000}_{-0.0000}$
210701761	3451	0.88	$0.0152^{+0.0089}_{-0.0052}$	$1.82^{+0.50}_{-0.42}$	$0.0005^{+0.0000}_{-0.0000}$	$0.0075^{+0.0042}_{-0.0019}$	$1.21^{+0.61}_{-0.25}$	$0.0005^{+0.0000}_{-0.0000}$
210708529	3538	7.16	$0.0094^{+0.0058}_{-0.0030}$	$1.49^{+0.46}_{-0.32}$	$0.0012^{+0.0001}_{-0.0000}$	$0.0105^{+0.0032}_{-0.0026}$	$2.59^{+0.28}_{-0.45}$	$0.0006^{+0.0000}_{-0.0000}$
210711240	3500	6.11	$0.0012^{+0.0004}_{-0.0002}$	$0.99^{+0.15}_{-0.12}$	$0.0001^{+0.0000}_{-0.0000}$	$0.0034^{+0.0010}_{-0.0008}$	$2.64^{+0.25}_{-0.42}$	$0.0001^{+0.0000}_{-0.0000}$
210715947	4000	7.39	$0.0046^{+0.0037}_{-0.0016}$	$1.41^{+0.52}_{-0.34}$	$0.0003^{+0.0000}_{-0.0000}$	$0.0054^{+0.0016}_{-0.0013}$	$2.63^{+0.26}_{-0.41}$	$0.0001^{+0.0000}_{-0.0000}$

Table 5
(Continued)

EPIC ID	Temperature [K] (1)	Period [day] (2)	h_{04}	w_{04}	σ_{04}	h_{13}	w_{13}	σ_{13}
210717184	3679	7.24	$0.0013^{+0.0008}_{-0.0004}$	$1.44^{+0.98}_{-0.68}$	$0.0005^{+0.0000}_{-0.0000}$	$0.0049^{+0.0025}_{-0.0015}$	$1.81^{+0.62}_{-0.47}$	$0.0002^{+0.0000}_{-0.0000}$
210718930	3504	2.41	$0.0085^{+0.0046}_{-0.0025}$	$1.57^{+0.64}_{-0.35}$	$0.0006^{+0.0000}_{-0.0000}$	$0.0074^{+0.0022}_{-0.0011}$	$0.46^{+0.53}_{-0.03}$	$0.0005^{+0.0002}_{-0.0000}$
210734946	3550	0.20	$0.0047^{+0.0017}_{-0.0013}$	$2.39^{+0.43}_{-0.61}$	$0.0009^{+0.0000}_{-0.0000}$	$0.0037^{+0.0023}_{-0.0013}$	$1.77^{+0.62}_{-0.46}$	$0.0006^{+0.0000}_{-0.0000}$
210740720	3625	0.46	$0.0076^{+0.0041}_{-0.0025}$	$1.90^{+0.62}_{-0.51}$	$0.0012^{+0.0001}_{-0.0000}$	$0.0104^{+0.0061}_{-0.0032}$	$1.54^{+0.41}_{-0.29}$	$0.0010^{+0.0000}_{-0.0000}$
210742017	3524	2.88	$0.0125^{+0.0033}_{-0.0025}$	$2.75^{+0.18}_{-0.33}$	$0.0004^{+0.0000}_{-0.0000}$	$0.0085^{+0.0028}_{-0.0021}$	$2.52^{+0.33}_{-0.46}$	$0.0003^{+0.0000}_{-0.0000}$
210754620	3512	0.63	$0.0119^{+0.0056}_{-0.0042}$	$2.18^{+0.51}_{-0.54}$	$0.0008^{+0.0000}_{-0.0000}$	$0.0090^{+0.0044}_{-0.0025}$	$1.32^{+0.28}_{-0.20}$	$0.0004^{+0.0000}_{-0.0000}$
210754930	3836	2.26	$0.0199^{+0.0081}_{-0.0049}$	$1.16^{+0.18}_{-0.14}$	$0.0009^{+0.0000}_{-0.0000}$	$0.0453^{+0.0229}_{-0.0125}$	$1.40^{+0.61}_{-0.30}$	$0.0020^{+0.0002}_{-0.0001}$
210786882	3700	2.99	$0.0021^{+0.0007}_{-0.0006}$	$2.45^{+0.38}_{-0.56}$	$0.0001^{+0.0000}_{-0.0000}$	$0.0012^{+0.0004}_{-0.0002}$	$1.02^{+0.19}_{-0.14}$	$0.0001^{+0.0000}_{-0.0000}$

References: (1): Huber et al. (2016), (2) GLS in this study.

ORCID iDs

Kohei Miyakawa https://orcid.org/0000-0002-5706-3497
Teruyuki Hirano https://orcid.org/0000-0003-3618-7535
Akihiko Fukui https://orcid.org/0000-0002-4909-5763
Andrew W. Mann https://orcid.org/0000-0003-3654-1602
Eric Gaidos https://orcid.org/0000-0002-5258-6846
Bun'ei Sato https://orcid.org/0000-0001-8033-5633

References

Adelman-McCarthy, J. K., et al. 2009, VizieR Online Data Catalog, II/294
Aigrain, S., Pont, F., & Zucker, S. 2012, MNRAS, 419, 3147
Allard, F., Homeier, D., Freytag, B., et al. 2013, MSAIS, 24, 128
Anglada-Escudé, G., Butler, R. P., Reiners, A., et al. 2013, AN, 334, 184
Artigau, É., Kouach, D., Donati, J.-F., et al. 2014, Proc. SPIE, 9147, 914715
Bean, J. L., Seifahrt, A., Hartman, H., et al. 2010, ApJ, 713, 410
Berdyugina, S. V. 2005, LRSP, 2, 8
Borucki, W. J., Koch, D., Basri, G., et al. 2010, Sci, 327, 977
Brandt, T. D., & Huang, C. X. 2015, ApJ, 807, 58
Catalano, S., Biazzo, K., Frasca, A., & Marilli, E. 2002, A&A, 394, 1009
Cui, X.-Q., Zhao, Y.-H., Chu, Y.-Q., et al. 2012, RAA, 12, 1197
Cutri, R. M., Skrutskie, M. F., van Dyk, S., et al. 2003, VizieR Online Data Catalog, II/246
Dahm, S. E. 2015, ApJ, 813, 108
Davenport, J. R. A., Hebb, L., & Hawley, S. L. 2015, ApJ, 806, 212
Douglas, S. T., Curtis, J. L., Agüeros, M. A., et al. 2019, ApJ, 879, 100
Evans, D. F. 2018, RNAAS, 2, 20
Foreman-Mackey, D., Hogg, D. W., Lang, D., & Goodman, J. 2013, PASP, 125, 306
Frasca, A., Biazzo, K., Tas, G., Evren, S., & Lanzafame, A. C. 2008, A&A, 479, 557
Frasca, A., Covino, E., Spezzi, L., et al. 2009, A&A, 508, 1313
Fukugita, M., Shimasaku, K., & Ichikawa, T. 1995, PASP, 107, 945
Fukui, A., Narita, N., Kurosaki, K., et al. 2013, ApJ, 770, 95
Fukui, A., Narita, N., Tristram, P. J., et al. 2011, PASJ, 63, 287
Gaia Collaboration, Brown, A. G. A., & Vallenari, A. 2018, A&A, 616, A1
Gaia Collaboration, Brown, A. G. A., Vallenari, A., et al. 2021, A&A, 649, A1
Gaia Collaboration, Prusti, T., de Bruijne, J. H. J., et al. 2016, A&A, 595, A1
Grunblatt, S. K., Howard, A. W., & Haywood, R. D. 2015, ApJ, 808, 127
Haywood, R. D., Collier Cameron, A., Queloz, D., et al. 2014, MNRAS, 443, 2517
Hirano, T., Fukui, A., Mann, A. W., et al. 2016, ApJ, 820, 41
Howell, S. B., Sobeck, C., Haas, M., et al. 2014, PASP, 126, 398
Huber, D., Bryson, S. T., Haas, M. R., et al. 2016, ApJS, 224, 2
Kim, Y.-C., & Demarque, P. 1996, ApJ, 457, 340
Kotani, T., Tamura, M., Nishikawa, J., et al. 2018, Proc. SPIE, 10702, 1070211
Kotani, T., Tamura, M., Suto, H., et al. 2014, Proc. SPIE, 9147, 914714
Luger, R., Foreman-Mackey, D., Hedges, C., & Hogg, D. W. 2021, arXiv:2102.00007
Mahadevan, S., Ramsey, L. W., Terrien, R., et al. 2014, Proc. SPIE, 9147, 91471G
Mann, A. W., Dupuy, T., Kraus, A. L., et al. 2019, ApJ, 871, 63
Mann, A. W., Feiden, G. A., Gaidos, E., Boyajian, T., & von Braun, K. 2015, ApJ, 804, 64
Mann, A. W., Gaidos, E., Mace, G. N., et al. 2016a, ApJ, 818, 46
Mann, A. W., Gaidos, E., Vanderburg, A., et al. 2017, AJ, 153, 64
Mann, A. W., Johnson, M. C., Vanderburg, A., et al. 2020, AJ, 160, 179
Mann, A. W., Newton, E. R., Rizzuto, A. C., et al. 2016b, AJ, 152, 61
Mann, A. W., Vanderburg, A., Rizzuto, A. C., et al. 2018, AJ, 155, 4
Martín, E. L., Lodieu, N., Pavlenko, Y., & Béjar, V. J. S. 2018, ApJ, 856, 40
McQuillan, A., Aigrain, S., & Mazeh, T. 2013, MNRAS, 432, 1203
Nagashima, C., Nagayama, T., Nakajima, Y., et al. 1999, in Star Formation, ed. T. Nakamoto (Nagoya: Nobeyama Radio Observatory), 397
Newton, E. R., Mann, A. W., Tofflemire, B. M., et al. 2019, ApJL, 880, L17
O'Neal, D., Saar, S. H., & Neff, J. E. 1996, ApJ, 463, 766
Obermeier, C., Henning, T., Schlieder, J. E., et al. 2016, AJ, 152, 223
Owen, J. E. 2019, AREPS, 47, 67
Panja, M., Cameron, R., & Solanki, S. K. 2020, ApJ, 893, 113
Paulson, D. B., Cochran, W. D., & Hatzes, A. P. 2004, AJ, 127, 3579
Pecaut, M. J., Mamajek, E. E., & Bubar, E. J. 2012, ApJ, 746, 154
Perryman, M. A. C., Brown, A. G. A., Lebreton, Y., et al. 1998, A&A, 331, 81
Queloz, D., Henry, G. W., Sivan, J. P., et al. 2001, A&A, 379, 279
Quirrenbach, A., Amado, P. J., Caballero, J. A., et al. 2016, Proc. SPIE, 9908, 990812
Rasmussen, C. E., & Williams, C. K. I. 2006, Gaussian Processes for Machine Learning (Cambridge, MA: MIT Press)
Reiners, A., & Basri, G. 2010, ApJ, 710, 924
Reinhold, T., Reiners, A., & Basri, G. 2013, A&A, 560, A4
Ricker, G. R., Winn, J. N., Vanderspek, R., et al. 2015, JATIS, 1, 014003
Rizzuto, A. C., Newton, E. R., Mann, A. W., et al. 2020, AJ, 160, 33
Robertson, P., Mahadevan, S., Endl, M., & Roy, A. 2014, Sci, 345, 440
Robertson, P., Stefansson, G., Mahadevan, S., et al. 2020, ApJ, 897, 125
Rodono, M., Cutispoto, G., Pazzani, V., et al. 1986, A&A, 165, 135
Stassun, K. G., & Torres, G. 2021, ApJL, 907, L33
Stauffer, J. R., Jones, B. F., Backman, D., et al. 2003, AJ, 126, 833
Strassmeier, K. G. 2009, A&ARv, 17, 251
Tal-Or, L., Zechmeister, M., Reiners, A., et al. 2018, A&A, 614, A122
Tamura, M., Suto, H., Nishikawa, J., et al. 2012, Proc. SPIE, 8446, 84461T
Zechmeister, M., & Kürster, M. 2009, A&A, 496, 577